Important Notice to Authors

Attached is a PDF proof of your forthcoming article in *Journal of Applied Remote Sensing*.

No further publication processing will occur until we receive your response to this proof. Please respond within 48 hours of receipt of this message.

Questions & Comments to Address

Please see the back page of this PDF proof for an itemized list of questions and comments to be addressed. The numbers listed correspond to numbers in the margin of the proof pages pinpointing the source of the question and/or comment. The numbers will be removed from the margins prior to publication.

Other Items to Check

- Please check your title, author list, and acknowledgments carefully for any omissions or errors. Also check all text, illustrations, captions, equations, tables, references, and author biographies thoroughly. If you are adding biographies, note that they should not exceed 75 words each. Authors are encouraged to upload photographs and update their online SPIE profile on our website at http://spie.org/app/profiles/default.aspx.
- Please proofread the article very carefully. This will be your only opportunity to provide corrections. Note that responsibility for detecting errors lies with the author.
- Please check that your figures are accurate and sized properly. Figure quality in this proof is representative of the quality to be used in the online journal. To achieve manageable file size for online delivery, some compression and downsampling of figures may have occurred. Fine details may have become somewhat fuzzy, especially in color figures. The print journal uses files of higher resolution and therefore details may be sharper in print.

Ways to Respond

- Web: If you accessed this proof online, follow the instructions on the web page to submit corrections.
- Email: Send corrections to spie-manager@luminad.com. Include the paper number for your article in the subject line.

Forms

The *Journal of Applied Remote Sensing* offers the option of open access publication for a flat fee of $960 ($660 for Letters). Open access papers will be published under a Creative Commons CC BY 3.0 license. Authors who do not pay for open access will be published under the standard SPIE Transfer of Copyright agreement.

- Pay the open access fee online at http://spie.org/publications/journals/pubcharges.
- If you haven't already, complete the appropriate publication license online by logging into your account at http://jars.msubmit.net.

If You Need to Contact Us

You may send an email message to spie-manager@luminad.com. Please reference the paper number and the first author of your article in your subject line. We will respond to you via email as quickly as possible.

Evapotranspiration estimation using Landsat-8 data with a two-layer framework

Jian Yin,[a,b,c,]* Hailong Wang,[d] Chesheng Zhan,[b] and Yang Lu[c,e]
[a]Northeast Agricultural University, School of Water Conservancy and Civil Engineering, Harbin, China
[b]Chinese Academy of Science, Key Laboratory of Water Cycle and Related Land Surface Processes, Institute of Geographic Science and Natural Resource Research, Beijing, China
[c]Anqing Normal University, School of Resources and Environment, Anqing, China
[d]University of Aberdeen, Northern Rivers Institute, School of Geosciences, Aberdeen, United Kingdom
[e]Ningbo University, Department of Geography and Spatial Information Techniques, Anqing Normal University, Ningbo, China

Abstract. Evapotranspiration (ET) plays an important role in hydrological cycle by linking land surface and atmosphere through water and energy transfers. Based on the data from the Landsat-8 satellite for typical days with clear sky condition from 2013 to 2016, a two-layer daily ET remote sensing framework was built, which includes four compartments: surface feature parameter estimation, evaporative fraction estimation, daily net radiation estimation, and daily ET extension. Based on the model, evaporation, transpiration, and daily ET in Shahe River Basin were estimated. The estimated daily ET showed a mean absolute percentage error of 8.7% in the plain areas, and 12.1% in the mountainous areas, compared to observations using large aperture scintillometer and eddy covariance system. The method gave higher accuracy than other remote sensing models applied in the same area previously, including the surface energy balance system and the ETWatch. By analyzing the relationship between land use types and surface water/heat fluxes, it was found that the surface energy balance components in the basin have prominent spatial-temporal features, and the soil component's features are more obvious. It indicated that the proposed two-layer approach is superior to others in terms of simulation accuracy, and applicable to daily scale ET estimations on complex terrains. © *2017 Society of Photo-Optical Instrumentation Engineers (SPIE)* [DOI: 10.1117/1.JRS.11.XX.XXXXXX]

1 Introduction

Evapotranspiration (ET) that consists of evaporation and transpiration determines interactions and feedbacks among geosphere, biosphere, and atmosphere in the earth system.[1–3] It is one of the most difficult components to estimate in the terrestrial water budgets, and accurate ET estimation is crucial to understanding the land–atmosphere interactions to mediate climate change impacts, and improving water resources management, agricultural production assessment, and environmental protection.[4,5] Therefore, ET estimation is listed as a critical content of research on land–atmosphere interactions and agricultural irrigation and drainage by many international programs and organizations, such as the International Hydrological Programme, the United Nations Environment Programme, the International Geosphere and Biosphere Plan, and the United Nations Food and Agriculture Organization.

The physics of ET is now well understood,[6,7] yet we still face difficulties in its accurate estimation. Field techniques are able to give ET fluxes in a relatively high accuracy, but

---

*Address all correspondence to: Jian Yin, E-mail: yinjinbnu@163.com

they usually are limited in space and time,[8,9] and hard to be extrapolated to regional estimation.[10] On the other hand, remote sensing methods emerging from around the 1960s provide a means to quantify ET at both bigger spatial scales and longer temporal scales.[11] Remote sensing ET models are based on energy balance equation, and through years of development, their capability to estimate ET over heterogeneous land surface has been improved.[12] Generally, such remote sensing models can be divided into one-layer and two-layer models.[13] One-layer models take land surface as one entity thus fail to distinguish soil evaporation from vegetation transpiration;[14] they perform better in regions with a moist climate or dense vegetation cover than areas with dry climate and sparse vegetation cover. Whereas two-layer models target bare soils and vegetated surfaces at the same time, so they are able to partition ET into soil evaporation and vegetation transpiration,[15] therefore, they are favorable for the understanding of biomass production and water use efficiency, etc.

Land surface temperature is one important input for remote sensing ET algorithms. Usually temperatures of soil and vegetation are unequal; water and heat exchanges among soil, vegetation, and the atmosphere do not take place on an identical boundary surface.[16,17] According to the two-layer model, soil and vegetation temperatures that can be directly acquired by a multiangle thermal infrared sensor (TIRS) should serve as driving forces.[18] However, most sensors are single-angled. To overcome the limitations of single-angle thermal infrared band data, Norman et al.[19] developed a parallel model that can be employed to estimate surface fluxes in large spatial areas based on a two-source model by Shuttleworth and Wallace.[20] The parallel model takes advantage of Beer's law to decompose the net radiation for vegetation canopy and underlying soil, and Priestley–Taylor formula to partition soil and vegetation temperatures for sensible and latent heat fluxes calculations. Over the last decade, this model has been verified under diverse vegetation cover conditions.[21] In the meantime, many studies use the triangle/trapezoidal method to partition temperatures based on single-angle remote sensing data through determination of dry and wet limits[13,22,23] by scatter plots of land surface temperature and normalized difference vegetation index (NDVI). As a result, constraints from multiangle data are diminished.[24] The simple remote sensing ET model (Sim-ReSET)[25,26] and the pixel ranking-layered energy segmentation model[27,28] are typical examples. In addition, they assumed that temperature at a reference altitude is approximately equal to the vegetation temperature. Similarly, for the pixel ranking-layered energy segmentation model,[27,28] the pixel component arranging and comparing algorithm (PCACA) is proposed to decompose component temperature based on envelope curves in scatter plot of surface temperature and fractional vegetation cover. Layered energy segmentation algorithm (LESA) is further constructed with the combination of Bowen ratio to calculate net radiation components of soil and vegetation. In recent years, with the continuous improvement of the PCACA-LESA algorithm, it is more operational in terms of computing.[29,30] Based on the PCACA-LESA, regional instantaneous evaporative fraction is estimated in this paper. Moreover, in combination with an improved total daily net radiation estimation (DNRE) model and the daily evaporation scale extension module, a two-layer remote sensing inversion system is established to estimate the daily land surface ET. Taking Shahe River Basin in Beijing as an example, we estimated ET on 33 clear days in different seasons between 2013 and 2016. Results were compared to field observations of the large-aperture scintillometer and eddy covariance (EC) system. The results help improve our understanding of the water cycle in the basin.

2 Materials and Methods

2.1 Study Site

Shahe River Basin of Beijing, located at 40°00′N-40°30′N and 115°50′E-116°20′E, is a subcatchment of Haihe River Basin. Within a semihumid climate zone in North China, elevation gradient of this basin is 1309 m (Fig. 1). Forests cover about 48% of the basin, and cultivated lands around 35%. The main stream flows from Northwest to Southeast; in detail, the mountainous upstream is covered by forest, while farm lands and urban areas are dominant in the downstream. With four distinctive seasons, soil exposure shows different proportion and characteristics spatially. In recent years, rainfall keeps decreasing, especially from 2005 to 2015, the mean annual precipitation is 427.5 mm, decreased dramatically compared to 602 mm from 1956 to 2015.
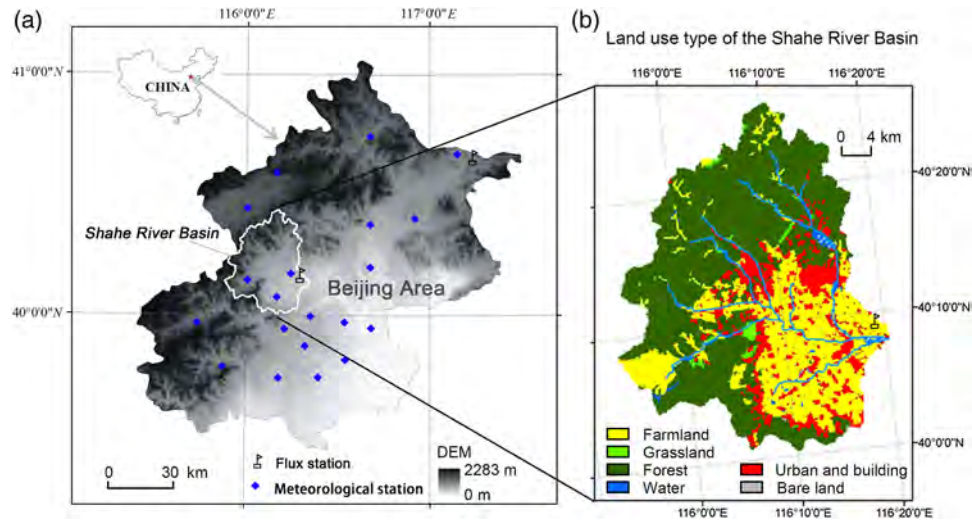
Fig. 1 Map of the study area. (a) The location of instrumentation and elevation and (b) the land use map.

Table 1 The 33 days with data obtained from the OLI/TIRS of Landsat-8.

	Date
OLI/TIRS (Landsat-8)	2013/5/12, 2013/6/13, 2013/7/31, 2013/9/1, 2013/10/3, 2013/11/4, 2013/11/20, 2013/12/6, 2014/4/13, 2014/4/29, 2014/5/15, 2014/8/19, 2014/9/4, 2014/10/6, 2014/12/25, 2015/1/10, 2015/2/11, 2015/3/15, 2015/4/16, 2015/5/2, 2015/5/18, 2015/7/5, 2015/8/22, 2015/9/7, 2015/9/23, 2015/11/26, 2016/2/14, 2016/3/1, 2016/4/18, 2016/5/4, 2016/5/20, 2016/8/8, 2016/9/9

2.2 Data

Field observations include surface flux stations and meteorological data such as air temperature, wind speed, atmospheric pressure, radiation, and humidity (locations are shown in Fig. 1). The meteorological data are interpolated at a spatial resolution of 30 m. Remote sensing data are derived from operational land imager (OLI) (bands 1 to 9) and TIRS (bands 10 and 11) with a preferable imaging quality acquired by Landsat-8 on 33 days (Table 1). The original spatial resolution of the OLI imagery is 30 m, and 100 m for TIRS. The DEM and geographic information data from land use map and soil-type map are provided by Data Center for Resources and Environmental Sciences of China Academy of Sciences. All the data involved in ET estimation are transformed into 30-m spatial resolution under UTM-GWS84 projection.

2.3 Methods

The two-layer daily ET remote sensing system (TDERSS) in this study contains four modules: surface feature parameter inversion module (SFPI), instantaneous evaporative fraction estimation module (IEFE), the DNRE module, and the daily ET extension module (DEE). The SFPI is used to estimate fractional vegetation cover, land surface albedo, temperature, and emissivity required in the IEFE, which is based on PCACA-LESA.[27,28] The IEFE calculates the latent heat flux, sensible heat flux, net radiation, soil heat flux, and instantaneous evaporative fraction. The DNRE is based on empirical formula to obtain daily net radiation. Finally, daily ET is obtained by the DEE through the evaporative fraction method.[31] The detailed flowchart of the TDERSE is shown in Fig. 2. Details of each module are given below.
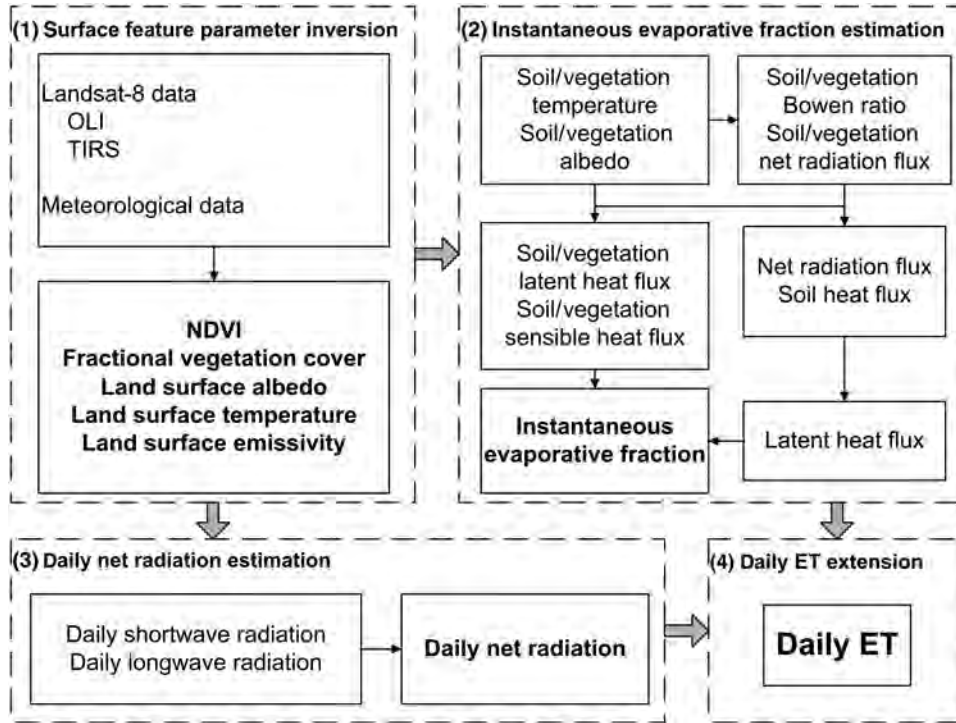
Fig. 2 Flowchart of the daily ET remote sensing estimation methodology.

2.3.1 *Surface feature parameter inversion*

Fractional vegetation cover, surface albedo, surface temperature, and surface emissivity are the driving data of the PCACA-LESA.

Fractional vegetation cover and land surface albedo. The NDVI is calculated from reflectance data of OLI bands 4 to 5 after atmospheric and geometric corrections; fractional vegetation cover f is then obtained with the modified dimidiate pixel model.[32] Surface albedo α is estimated using the method in Liang[33] with surface reflectance data from OLI bands 2 to 8.

Land surface temperature. The monowindow algorithm dependent on surface heat radiation transfer equation is employed[34] to infer surface temperature for Shahe River Basin using TIRS data. The relevant equations are given as follows.

Brightness temperature T_{10} is calculated according to the thermal infrared band 10.[34]

$$T_{10} = K_2 / \ln(1 + K_1 / \rho^{b10}), \qquad (1)$$

where ρ^{b10} refers to reflectance of the 10th band of Landsat-8, considering the USGS calibration notices,[35] ρ^{b10} could be calculated based on the metadata file of Landsat-8 data;[34] K_1 and K_2 are constants preset before satellite launch ($K_1 = 774.89$ W $\cdot$ m^{-2} $\cdot$ sr^{-1} $\cdot$ μm^{-1} and $K_2 = 1321.08$ K). Brightness temperature is different from actual surface temperature and the gap is about 5 to 10 K for on a dry clear day.[36] Therefore, the brightness temperature should be corrected[34] to calculate the surface temperature T_m.

$$T_m = \{A \cdot F + [(B-1)F + 1]T_{10} - D \cdot T_x\}/C, \qquad (2)$$

where A and B are constants; when surface temperature ranges from 273.15 to 343.15 K, $A = -67.355351$, $B = 0.458606$; in addition, $C = \zeta \cdot \tau$, $D = (1 - \tau)[1 + (1 - \zeta)\tau]$, and

Table 2 NDVI-based land use classification.

Classification	Criteria
Vegetation	NDVI≧0.5
Building lot	OLI7≧OLI6, OLI7≧OLI5, and sum for band OLI2 to OLI7 is larger than 900. NDVI is 0.1, as a threshold to differentiate
Vegetation in building lot	building lot and vegetation in building lot.
Bare land	OLI5≧OLI6, OLI5≧OLI4, and the sum for band OLI2 to OLI7≦900. NDVI = 0.15, serve as the threshold to
Vegetation in bare land	distinguish bare land and vegetation in bare land.
Water body	NDVI = 0; and, OLI5≦OLI4.

$F = 1 - C - D$. T_x denotes atmospheric mean temperature (K), while ζ and τ are land surface emissivity and atmospheric transmissivity, respectively. $T_x = 1.60110 + 092621T_0$, where T_0 is the near-surface air temperature (K). If the total atmospheric water vapor content w lies between 0.4 and 1.6 g/cm^2, τ can be calculated as $\tau = 0.974290$ to $0.08007\ w$; if w varies between 1.6 and 3.0 g/cm^2, $\tau = 1.031412$ to $0.11536\ w$. Empirical equation between effective water vapor content of the atmosphere in the research area and ground water vapor pressure can be described as follows:

$$w = 0.185 + 0.144e, \tag{3}$$

where e is the actual water vapor pressure on surface (hPa).

Land surface emissivity. In order to calculate the land surface emissivity, land use types are classified into six categories based on NDVI, including vegetation, water body, bare land, vegetation in bare land, building lot, and vegetation in building lot. Classification methods are presented in Table 2.

We took emissivity values from Tian et al.,[29] that is, 0.986 for vegetation, 0.995, 0.972, and 0.97 for water body, bare land, and building correspondingly. Emissivity in pixels mixed of soil and vegetation is calculated from Eq. (4), and in pixels mixed with vegetation and building lot calculated from Eq. (5).

$$\varepsilon_m = fR_v\varepsilon_v + (1-f)R_s\varepsilon_s + d\varepsilon, \tag{4}$$

$$\varepsilon_m = fR_v\varepsilon_v + (1-f)R_b\varepsilon_b + d\varepsilon, \tag{5}$$

where R is the temperature scaling function; the subscripts v, s, and b represent vegetation, soil, and building. R is defined as $R_i = (T_i/T)^4$ in which i stands for v, s, and b, T for surface temperature (K). In areas where land surface is relatively flat, thermal radiation interactions ($d\varepsilon$) between the two surfaces are very weak and thus $d\varepsilon = 0$.

2.3.2 *Instantaneous evaporative fraction estimation*

The instantaneous evaporative fraction Λ of land surface can be defined as follows:

$$\Lambda = \lambda E/(R_n - G), \tag{6}$$

where λE is surface latent heat flux, while R_n and G are net radiation flux and soil heat flux. Empirical relation between soil heat flux and net radiation flux of land surface is presented as

$$G \approx 0.3(1 - 0.9f)R_n. \tag{7}$$

In this paper, λE and R_n are estimated by the PCACA model to acquire instantaneous evaporative fraction Λ. In line with PCACA, combining measured values of parameters for dry and wet pixels, actual temperatures of four extreme mixed pixels are calculated according to "surface temperature-fractional vegetation cover" plot trapezoid envelope. Then, linear interpolation method is applied to obtain the relationship between land surface temperature and temperature of soil (T_s) and vegetation (T_v). Partitioning of surface temperature into soil and vegetation canopy temperature is given as

$$\delta\varepsilon_m T_m^4 = \delta\varepsilon_v T_v^4 + \delta\varepsilon_s(1-f)T_s^4, \tag{8}$$

where ε_m, ε_v, and ε_s refer to emissivity of mixed pixels, vegetation, and soil surface; σ to Boltzmann constant, and f to the fractional vegetation cover of mixed pixels. Derivation of f is performed from Eq. (8), together with simplifications, and the following equation can be achieved:

$$dT_m/df \approx T_v - T_s, \tag{9}$$

where dT_m/df is the slope of medium soil moisture content line in the trapezoid framework. "Theoretical dry boundary" is determined by reverse-reasoning calculations based on the energy balance method; "theoretical wet boundary" is determined by surface temperature over large water body (refer to Refs. 28 and 29). In the same manner, surface albedo α can also be decomposed into vegetation albedo α_v and soil albedo α_s.

In the LESA method, soil and vegetation Bowen ratio β_s or β_v are obtained first;[37,38] and then energy balance method is applied to partition available surface energy for soil evaporation and vegetation transpiration. Afterward, in combination with the trapezoid framework, Bowen ratio is figured out using Eq. (10), in which T_{SH} and T_{SL} are the maximum and minimum soil temperatures of pixels with identical coverage in the research area; β_{Si} and T_{Si} refer to soil Bowen ratio and soil temperature of a single pixel.

$$\beta_{Si} \approx (T_{SH} - T_{SL})/(T_{SH} - T_{Si}) - 1. \tag{10}$$

R_{sn} and R_{vn} that stand for net radiation fluxes of soil and vegetation are calculated from long-/short-wave radiations of soil/vegetation surfaces; then, linear mixture theory is applied to get the net surface radiation flux R_n through coverage weighting.[38]

$$R_n = fR_{vn} + (1-f)R_{sn}. \tag{11}$$

Lastly, instantaneous soil evaporation λE_s and instantaneous vegetation transpiration λE_v can be estimated.

$$\lambda E_s = (R_{sn} - G)/(1 + \beta_s), \qquad \lambda E_v = R_{vn}/(1 + \beta_v), \tag{12}$$

$$\lambda E = f\lambda E_v + (1-f)\lambda E_s. \tag{13}$$

2.3.3 Daily net radiation estimation

The daily net surface radiation denoted by R_d is the effective energy absorbed by land surface; it is equal to the sum of R_s and R_l, known as daily net short-wave radiation and daily net long-wave radiation.[39] R_s can be computed by R_{sun} (daily surface solar radiation) and α (surface albedo); that is, $R_s = (1-\alpha)R_{sun}$. R_{sun} is calculated based on the extraterrestrial radiation and the empirical parameters for atmospheric transmissivity.[40]

$$R_{sun} = (a_s + b_s \cdot n/N)W_d, \tag{14}$$

where n refers to the actual sunshine duration, N to the maximum sunshine duration, n/N to the relative sunshine duration (0 to 1), W_d is the daily extraterrestrial radiation (MJ $\cdot$ m^{-2} $\cdot$ day^{-1}),

and a_s and b_s are empirical regression coefficients taken as 0.56 and 0.16.[41] Daily extraterrestrial radiation (W_d) is computed as

$$W_d = (D/\pi)(1/\rho_0)^2 I_0(\omega_0 \sin \varphi \sin \delta + \cos \varphi \cos \delta \sin \omega_0), \tag{15}$$

where D is time span of a day; I_0 is solar constant (0.082 MJ m^{-2} min^{-1}); ω_0 corresponds to solar hour angle; φ (rad) and δ (rad) are geographic latitude and solar declination; and, $(1/\rho_0)^2$ is the earth–sin distance correction coefficient.

The Penman, Howard–Lloyd, and total radiation calculation methods are applied for daily net long-wave radiation calculation. When water vapor pressure ranges from 0 to 12.25 hPa, the total radiation calculation equation is selected [Eq. (16)]; if it ranges from 12.25 to 27.04 hPa, the Howard–Lloyd equation is selected [Eq. (17)]; otherwise, Penman equation is selected [Eq. (18)].

$$R_l = \varepsilon \delta T_0^4 \left(0.39 - 0.058 \sqrt{e_d} \right) \quad (0.1 + 0.9 \cdot n/N), \tag{16}$$

$$R_l = \varepsilon \delta T_0^4 \left(0.32 - 0.026 \sqrt{e_d} \right) \quad (0.3 + 0.7 \cdot n/N), \tag{17}$$

$$R_l = \varepsilon \delta T_0^4 \left(0.56 - 0.079 \sqrt{e_d} \right) \quad (0.1 + 0.9 \cdot n/N), \tag{18}$$

where T_a denotes the temperature (K), e_d is the average vapor pressure (hPa), n is the sunshine duration, and N is the maximum sunshine duration (hours).

2.3.4 *Daily ET extension*

The evaporative fraction is assumed to be constant during a day,[31] then the ratio between latent heat flux (λE) and available energy ($R_n - G$) is stable within a day.

$$\lambda E_d / F_d \approx \lambda E / F = \Lambda = \lambda E / (R_n - G), \tag{19}$$

where Λ refers to the instantaneous evaporative fraction. In addition, based on the calculated R_d, 24-h integral is carried out for Eq. (19) to achieve the daily ET.

$$E_d = \Lambda \cdot \frac{R_d}{\lambda}, \tag{20}$$

where E_d is the actual daily ET with a unit of mm $\cdot$ day^{-1}; R_d is the daily net radiation (unit: MJ $\cdot$ m^{-2} $\cdot$ day^{-1}); λ is the latent heat of vaporization (MJ $\cdot$ m^{-3}); and $\lambda = (2.501 - 0.02361 \times T_0) \times 10^3$ MJ $\cdot$ m^{-3}; T_0 is daily average temperature (°C).

2.3.5 *Validations*

Two validations were conducted here. First, observation data from the Xiaotangshan Flux Observation Station within the research area and ET results in the relevant pixels are selected for validation. Observation values from Miyun Flux Observation Station near the Shahe River Basin are also used for validation. Data from daytime observation stations consist of daily evaporation obtained through daily scale transformation of instantaneous fluxes measured by EC system and large aperture scintillometer. According to the previous studies,[29,42] in the case that surface energy balance equation closure [$\eta = (H + \lambda E)/(R_n - G)$] is larger than 0.8, the achieved simulation results have a high confidence level. Energy closures of simulation results are all higher than 0.8 on the 33 typical days in this study. Therefore, daily ET estimated by remote sensing inversion are in agreement with observations.

Second, we compared our ET results with another two commonly used remote sensing methods. The surface energy balance system (SEBS)[43] is a one-layer ET remote sensing model. According to China's specific regional characteristics, improvements have been made to the original SEBS model. The SEBS-China[9] was proved as a more appropriate model for estimating China's regional ET. In addition, with the support of Global Environment Facility, a number of ground flux stations have been established in the Haihe River Basin (including the Shahe River Basin).[44] Based on those studies, ETWatch[44] an integrated ET remote sensing system, was constructed by coupling the Penman–Monteith model and the "residue approach" of the surface energy balance equation. For the remote sensing data (30 m), the ETWatch adopts the calibrated and improved METRIC[45]/SEBAL[46] models; for 1-km data, it adopts the SEBS model. Recently, the ET estimation studies using ETWatch showed satisfactory results.[44,47,48] For example, using the 30 m TM data and the 1-km MODIS data in sunny days during 2002 to 2009, Jia et al.[47] estimated the daily ET, and used the observation data of Miyun, Guantao, and Daxing flux stations for validation. Wu et al.[48] fused the TM and MODIS data, and employed the ETWatch to calculate the daily ET in 30-m spatial resolution.

3 Results and Discussions

3.1 *Surface Parameters*

In the two-layer daily ET remote sensing system TDERSS, inputs include surface feature parameters including fractional vegetation cover, surface albedo, surface temperature, and surface emissivity. From Fig. 3, temperature, fractional vegetation cover, and emissivity variables
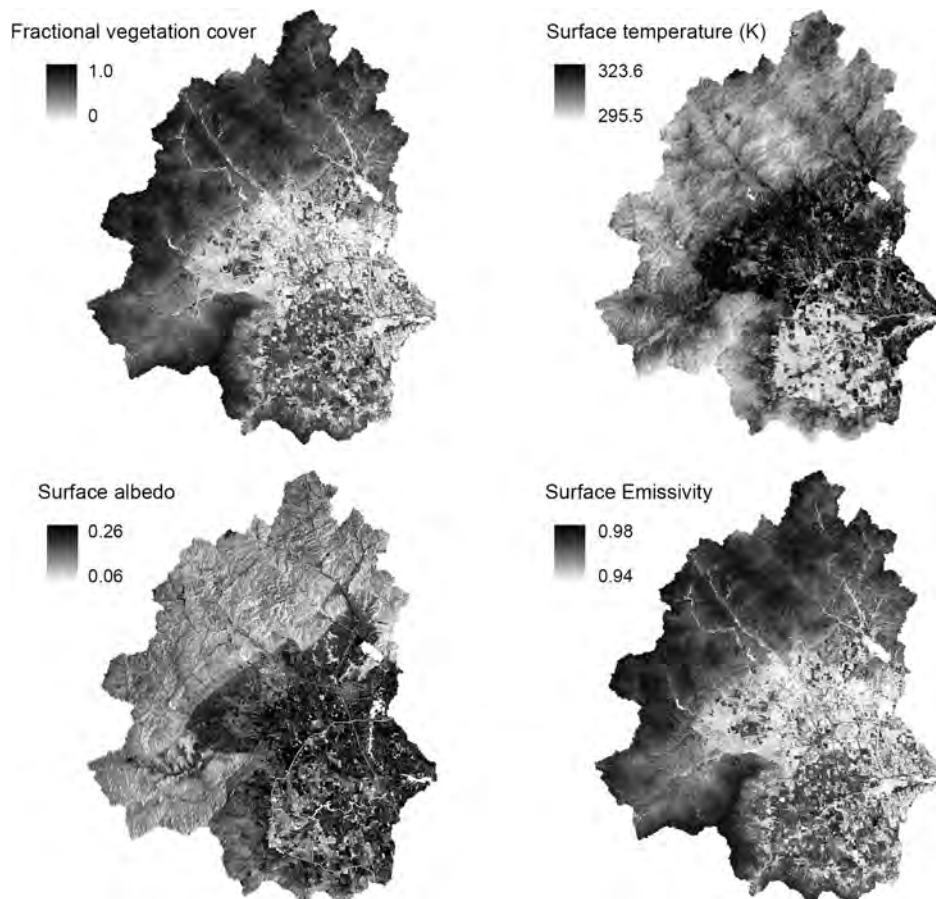

Fig. 3 Surface parameters of a typical day based on remote sensing (August 19, 2014).

are transitionally stable on up/downstream; and their transitional boundaries are inconspicuous. Fractional vegetation cover is the largest for mountainous areas, so is that of farm lands in plain areas. Changes in surface albedo in up/downstream as well as the plain area in the lower reaches are minor; a prominent boundary appears between mountainous areas on the upstream and the plain downstream for albedo.

3.2 *Evaporative Fluxes of Vegetation and Soil*

Flux inversion results of April 13, 2014, and October 6, 2014, are selected as representative spring and autumn days. According to the distribution diagram, surface flux inversion outcomes indicate that net radiation flux, soil heat flux, sensible heat flux, and latent heat flux have a good consistency with surface feature parameters in terms of the spatial distributions (Figs. 4–6).

Northwest of the area where fractional vegetation cover is high on the upstream, latent heat flux is greater than the downstream plain area on southeast; sensible heat flux on the lower reaches is larger than the upper reaches. The net radiation and soil heat flux on the upper reaches are larger than those on the lower reaches. The difference between the net radiation of the upper and lower reaches is small. For the soil heat flux, the difference of the data of the upstream and downstream is also trivial. However, for sensible heat flux, the contrast is more obvious. On the upstream, latent heat flux is relatively high while soil heat flux relatively low; on the downstream, the integral difference of them is not large.

At the moment of satellite passing, the average net radiation on representative day of spring is 605.8 and 637.6 W/m^2 in autumn. Differences among energy balance components in the lower and upper reaches are great on the representative day of spring; and they are minor in autumn. What needs to be pointed out is that in both spring and autumn, the basin has high average latent heat fluxes 221.3 and 279.1 W/m^2, respectively. The main reasons are that as in the crops leafing period, land surface is rather humid, solar radiation is strong, and evaporation is large in spring; and, in autumn, summer maize is still not harvested, together with unwithered grasses they contribute a considerable amount of surface evaporation. Average values of sensible heat fluxes of this basin in spring and autumn are 237.2 and 199.1 W/m^2. Land use types with a large sensible heat flux consist of building lot and dry bare land. In autumn, vegetation is denser than in spring on representative days, which leads to small specific surface area of bare soils; as a result, sensible heat flux in this period is lower than the representative day of spring.

Based on Figs. 3–6, soil and vegetation components of sensible and latent heat fluxes are both higher on the upstream than those on the downstream areas. Latent heat and sensible heat components in spring have a more prominent spatial variability than in autumn, while it is
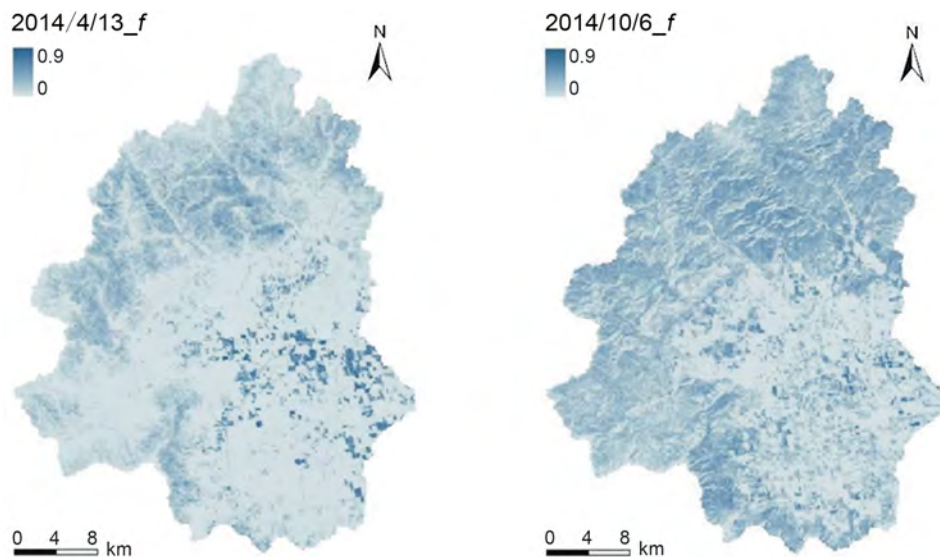

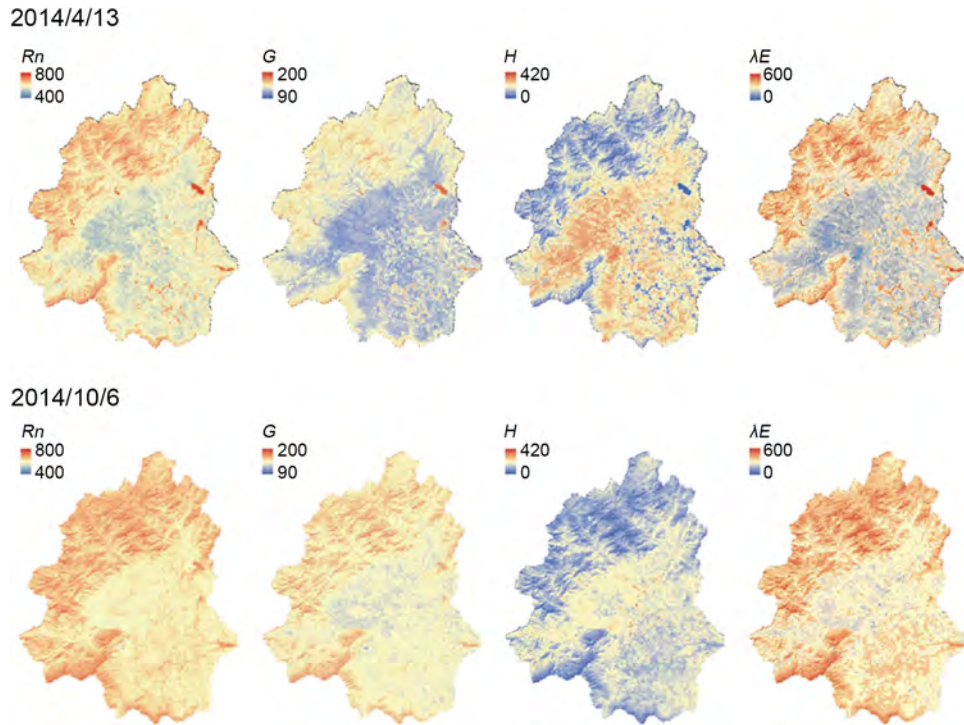**Fig. 4** Fractional vegetation cover distributions of Shahe River Basin in spring and autumn.

Fig. 5 Surface fluxes and relevant spatial distributions on typical days in spring and autumn. Units for energy fluxes are W/m².
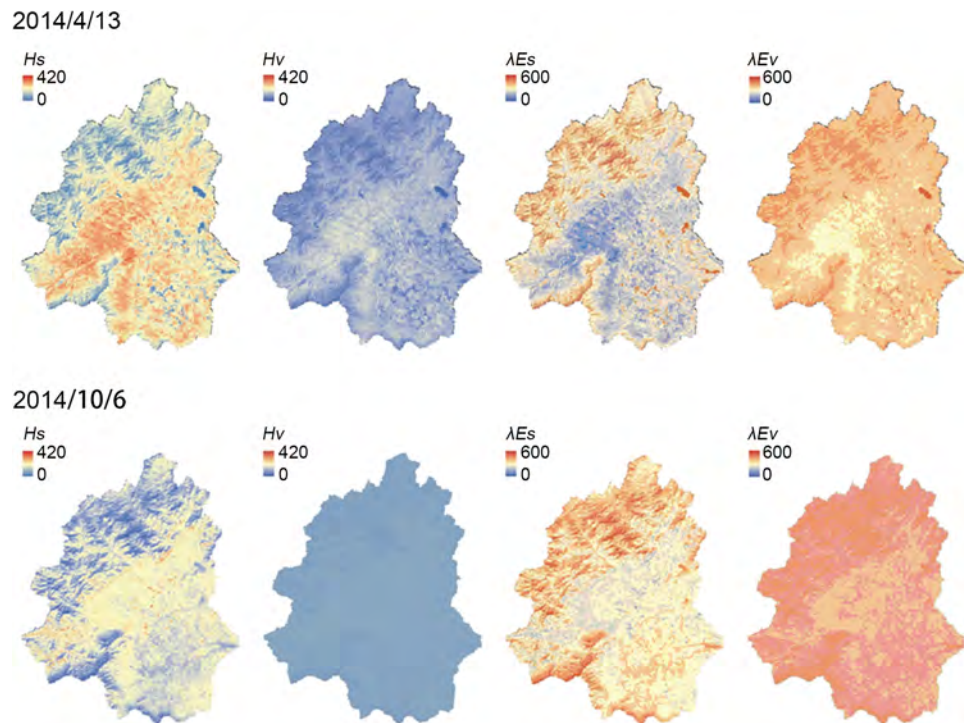
Fig. 6 The spatial distribution of soil/vegetation sensible and latent heat fluxes on typical days in spring and autumn.

insignificant for soil components in both spring and autumn. Soil and vegetation components for sensible heat flux in spring are both greater than those in autumn; however, latent heat flux components are lower than autumn. Soil component is greater than the vegetation component in total sensible heat and latent heat. In spring, sensible heat flux range and the mean value of soil are 0 to 420 and 244.9 W/m^2, which change to 1.5 to 421 and 212.3 W/m^2 in autumn. Moreover, the corresponding vegetation sensible heat ranges and mean values are 2 to 271, 154.1, and 78 to 130, 102.1 W/m^2, respectively. Regarding the minimum values for soil and vegetation components, sensible heat flux of soil is less than the vegetation. From the perspective of average value of the basin, latent heat of vegetation in spring is 309.3 and 214.3 W/m^2 of soil. In comparison, for autumn, they are 368.6 and 266.8 W/m^2.

Within the basin, latent heat flux and net radiation over a large reservoir are distinctly higher than other areas. According to surface fluxes in spring, the total latent heat fluxes between upstream and downstream areas are significantly different in spring. Regular-shaped patches with latent heat lower and sensible heat higher than other regions are distributed in a scattered manner in the lower reaches. Such patches are caused by winter wheat turning green, unseeded summer maize and nonuniformly developed vegetation canopy. In October, the Shahe River Basin enters its nongrowing season so that high value of sensible heat flux is substantially reduced (Figs. 3–6); especially for those near large water bodies, such a reduction becomes more distinct. At the same time, sensible heat flux around downstream water bodies goes down while the latent heat flux goes up.

3.3 Validation Results

3.3.1 Validation with the observations

For Xiaotangshan Station situated in cropland region on the lower reaches of Shahe River Basin, its underlying surface is dominated by crops (winter planting summer harvesting or summer planting autumn harvesting). Daily ET that varies between 0 and 3.5 mm reaches its peak at the end of spring to early summer. For comparison in Fig. 7, the relative error of daily evaporation simulation observations is between 0% and 20%, with a mean absolute percentage error (MAPE) of 8.7%, a mean relative error (MRE) of −1.0%, a correlation coefficient of 0.985, and a root-mean-square error of 0.776 mm. Thus, our remote sensing method estimates ET at a satisfactory accuracy level.

Miyun station is located at Xinchengzi Town, Miyun County in the northwest of Haihe River Basin, near the Shahe River Basin. The data of Miyun station are used as an alternative validation data for evaluating ET estimation in mountain area. It has a mixed underlying surface mainly formed by forest and crops in hilly region; in addition, vegetation is a mixture of needle-leaf and broadleaf; fruit trees and maize are primary crops, and the corn field is turned into bare land in the unfit planting time. Climatic characteristics and underlying surface features share similarities with the Shahe River Basin. Through spatial analysis, we selected the points with the similar underlying surface condition (elevation, slope, vegetation cover, land cover type, and
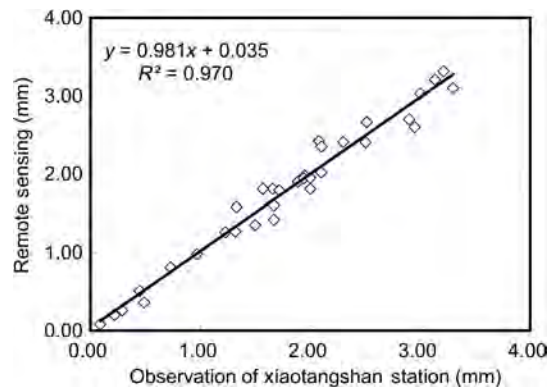

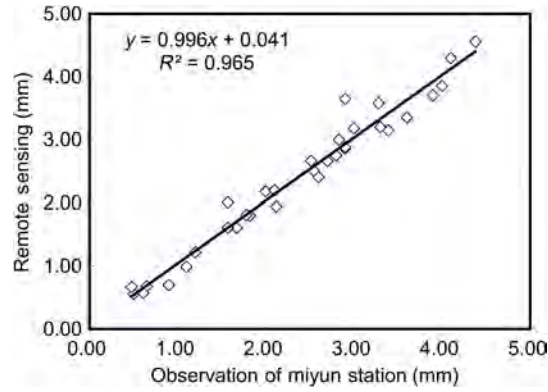**Fig. 7** Comparison of remote sensing daily ET and observations at the Xiaotangshan Station.

Fig. 8 Comparison of remote sensing daily ET and observations at the Miyun Station.

temperature) in the mountainous area of Shahe River Basin, and compared the average daily ET of them with the data by Miyun station. For comparison in Fig. 8, MAPE, MRE, root-mean-square error, and correlation coefficients is 12.1%, 3.3%, 1.20 mm, and 0.982 respectively.

3.3.2 *Intercomparison with other remote sensing models*

The comparisons of the daily ET results of TDERSS and SEBS-China models are given in Fig. 9.

The results show that the simulations of the two models are generally identical, with the MAPE of 13%. Compared with the daily ET values of corresponding pixels in the observation areas of flux stations, TDERSS has the advantage of accuracy over the SEBS-China. Because of the vegetation and soil-mixed farmland or forest in the area where the station is located, the bias may be due to nonseparated soil and vegetation of the SEBS-China. The difference between the daily ET by the two models was more significant in the growing season (April to October). In terms of the land use types, MAPE of SEBS and RSTM from low to high were water, grassland, forest, farmland, bare land, and building land.

Furthermore, Table 3 shows the statistics of the comparisons between the daily ET and the observations at the validation sites.

The MRE is the mean relative percentage error between the daily ET of remote sensing model and corresponding observation station. The MRE of the TDERSS is the smallest in growing seasons and all years. The MRE of TDERSS (30 m) is close to that of ETWatch in 1-km resolution. Overall, the TDERSS proposed in the study improved ET estimation accuracy compared to ETWatch and SEBS.
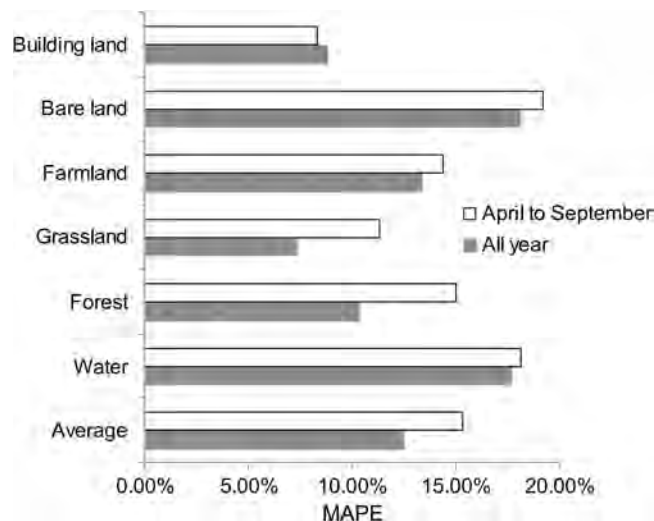

Fig. 9 Comparisons of daily ET results by TDERSS, SEBS-China in different land use areas.

Table 3 Comparisons of daily ET results by TDERS, SEBS-China, ETWatch, and observation stations.

Model	Data	Spatial resolution of daily ET	Mean relative error (%) to the stations		
			Xiaotangshan	Miyun	Average
SEBS-China	OLI/TIRS	30 m	−6.9(−12.5)	−10.5(−15.7)	—
TDERSS	OLI/TIRS	30 m	−1.0(1.9)	3.3(5.2)	—
ETWatch[47]	TM	30 m	N/A	N/A	−9.1(−22.9)
ETWatch[47]	MODIS	1 km	N/A	N/A	0.99(−1.13)
ETWatch[48]	Fused data	30 m	2.60(N/A)	N/A	N/A

Note: Numbers in parentheses are the statistics during growing seasons (April to September).

3.4 *Spatial-Temporal Analysis*

In this study, April 15, 2014, August 19, 2014, October 6, 2014, and January 1, 2015, are used as representative days among four seasons to perform the spatial-temporal analysis of ET, net radiation, and evaporative fraction. It is clear from Fig. 10 that spatial differences among evaporative fractions for all seasons are not big; although in spring and summer when fractional vegetation
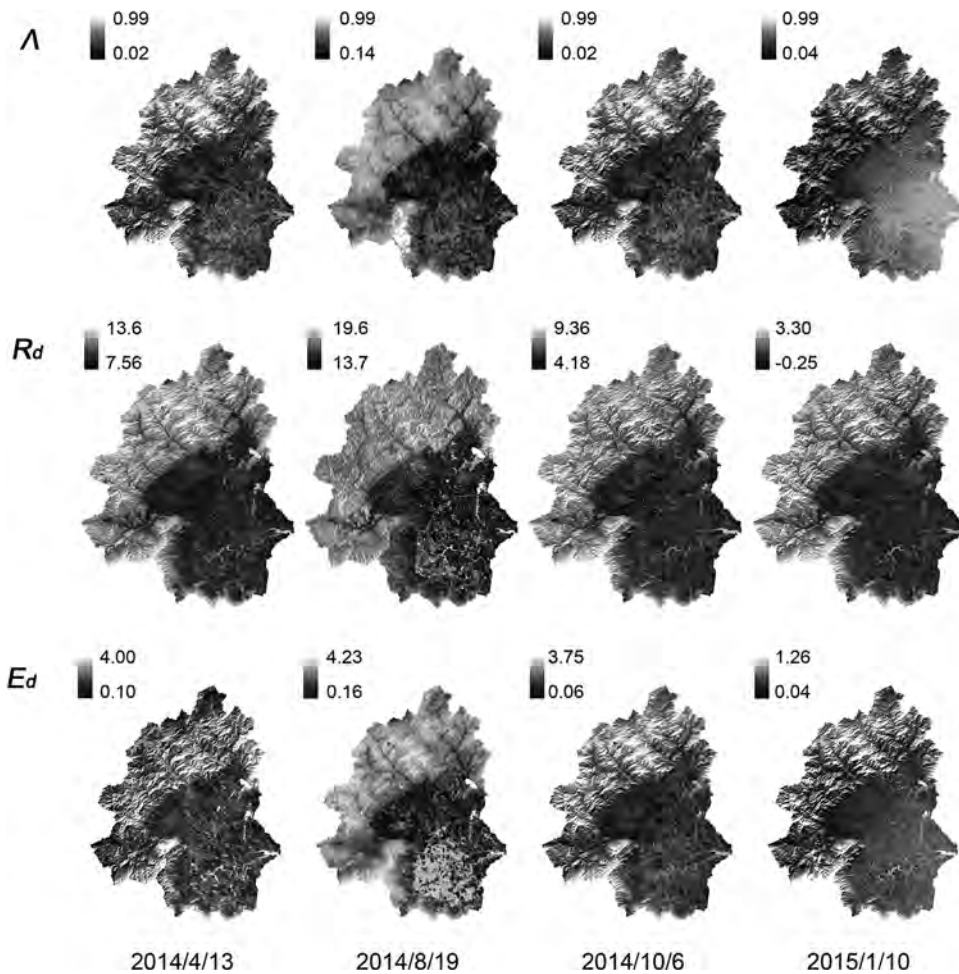

Fig. 10 Comparisons of daily net radiation (R_d), evaporative fraction (Λ), and daily ET (E_d) in the corresponding representative days in spring, summer, autumn, and winter.
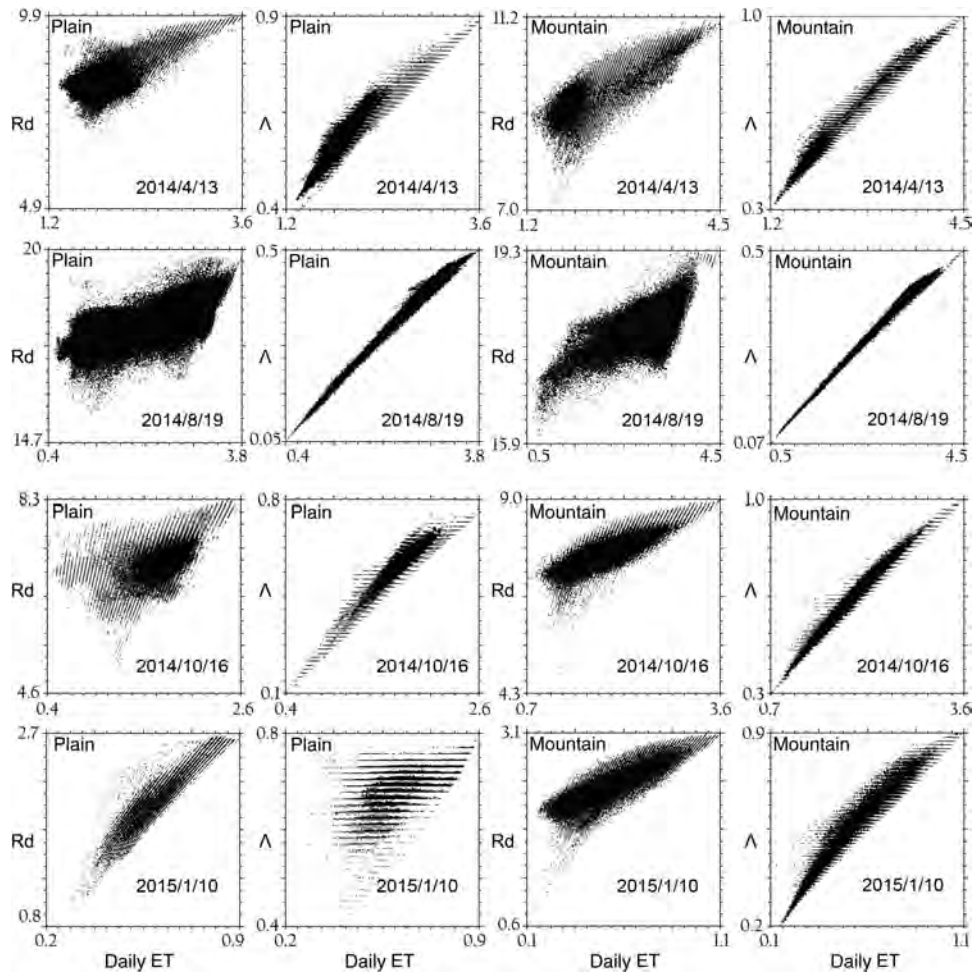
Fig. 11 Scatter plot of daily ET-evaporative fraction and daily ET-net radiation for plain area and mountain area across four seasons.

cover is high, the average evaporative fraction of the basin is slightly higher than the other two seasons. On the upper reaches, the evaporative fraction is universally larger than farmlands and settlement places on the lower reaches. On representative days of different seasons, the total daily net radiation of the basin is high in the upstream and low in the downstream.

For the convenience of analysis, considerations are given to upstream mountainous areas and downstream plain areas of the Shahe River Basin in a separate way. Mountainous areas are defined with an elevation more than 130 m. The region where land use type is nonforestry with a slope less than 4.28% is defined as plain area. A scatter plot of evaporative fraction, daily net radiation, and daily ET are extracted respectively for plain and mountainous areas, given in Fig. 11. Except plain area on representative days of winter, evaporative fraction and daily ET exhibit prominent linear relationships which indicates that a good correlation exists between daily ET and evaporative fraction. As mountainous areas in the Shahe River Basin have mingled forest of coniferous and broadleaf deciduous forest, scatter distribution of daily ET and evaporative fraction in four seasons tend to be uniform. However, due to impacts of vegetation density in the mountainous area, the correlation between daily ET and evaporative fraction is the strongest in summer, weakest for winter. For most plains dominated by farmlands and buildings, they are primarily covered by bare lands and sporadically distributed vegetation in winter. To sum up, under a circumstance of dense vegetation, daily ET and evaporative fraction are distinctly correlated; on the contrary, when vegetation is sparse, such a correlation is weak.

Similarly, relationships between daily ET and daily net radiation are also investigated for mountainous and plain areas. In four seasons, no matter in the mountainous area or the plain, correlation of daily ET and daily net radiation is not strong. The correlation between

ET and daily net radiation for plain in winter is the highest. In Shahe River Basin, there is very little rain in winter; and the plain area here is mainly dominated by bare lands; moreover, the major factor affecting daily ET is solar radiation. Therefore, such a preferable correlation exists between daily ET and daily net radiation in diverse regions of the plain. In summer, net radiation differences lie between farmlands on the downstream and forest in hilly region on the upstream are very minor. Evaporative fraction and daily ET are linearly related; however, the correlation between daily net radiation and daily ET is rather low. Thus, we can infer that major factor influencing seasonable variations of ET is net radiation; while underlying surface characteristics are also important to shape the ET spatial distributions. In general, fractional vegetation cover in mountainous area is larger than the plain area and it reaches the peak in summer. The relationships of daily ET, net radiation, and evaporative fraction can be summarized as follows: the higher the fractional vegetation cover, the greater the influence of evaporative fraction on the daily ET; the lower the fractional vegetation cover, the greater the influence of daily net radiation on daily ET.

4 Conclusions

Based on PCACA-LESA and ET extension algorithm, a remote sensing model TDERSS is constructed for daily ET estimation at 30-m spatial resolution. Application in the Shahe River Basin shows that the MAPE between our method and the EC and large-aperture scintillometer observations is 8.7% in plain areas and 12.1% in mountainous areas. Our model estimates more accurate ET than the ETWatch model and SEBS-China model. The results imply that our model is applicable for daily scale ET estimations on complex terrains. In addition, TDERSS is able to calculate the water/heat fluxes of soil and vegetation separately, which is helpful to study the process and space distribution of evaporation and transpiration.

Surface energy balance components in the Shahe River Basin have prominent spatial-temporal features. Instantaneous soil and vegetation water/heat fluxes are correlated to surface parameters of the basin. On sunny days of spring and autumn, spatial distribution of water/heat fluxes of vegetation and soils is uniform, despite that vegetation water/energy fluxes are slightly larger than soil, and the spatial variability of the latter is more prominent. Interannual variation of those distributions is minor and positively related to coverage within a year. The distribution of ET shows distinct patterns in the basin that upstream > downstream, forest lands > farmlands > building lots, summer > other seasons distinctly.

Acknowledgments

References

1. C. Cammalleri et al., "Actual evapotranspiration assessment by means of a coupled energy/hydrologic balance model: validation over an olive grove by means of scintillometry and measurements of soil water contents," *J. Hydrol.* **392**(1–2), 70–82 (2010).
2. R. Vinukollu et al., "Global estimates of evapotranspiration for climate studies using multi-sensor remote sensing data: evaluation of three process-based approaches," *Remote Sens. Environ.* **115**(3), 801–823 (2011).
3. Y. Yang et al., "Modeling evapotranspiration and its partitioning over a semiarid shrub ecosystem from satellite imagery: a multiple validation," *J. Appl. Remote Sens.* **7**(1), 073495 (2013).
4. X. Chen et al., "50-year evapotranspiration declining and potential causations in subtropical Guangdong province, Southern China," *Catena* **128**, 185–194 (2015).
5. C. Liu et al., "Spatial and temporal change in the potential evapotranspiration sensitivity to meteorological factors in China (1960-2007)," *J. Geogr. Sci.* **22**(1), 3–14 (2012).

6. B. Wu et al., "An improved method for deriving daily evapotranspiration estimates from satellite estimates on cloud-free days," *IEEE J. Sel. Top. Appl. Earth Obs. Remote Sens.* **9**(4), 1323–1330 (2016).

7. H. Li et al., "Temporal-spatial variation of evapotranspiration in the Yellow River Delta based on an integrated remote sensing model," *J. Appl. Remote Sens.* **9**(1), 096047 (2015).

8. C. Cammalleri and G. Ciraolo, "State and parameter update in a coupled energy/hydrologic balance model using ensemble Kalman filtering," *J. Hydrol.* **416**(2), 171–181 (2012).

9. C. Zhan et al., "Regional estimation and validation of remotely sensed evapotranspiration in China," *Catena* **133**, 35–42 (2015).

10. K. R. Knipper et al., "Evaluation of a moderate resolution imaging spectroradiometer triangle-based algorithm for evapotranspiration estimates in subalpine regions," *J. Appl. Remote Sens.* **10**(1), 016002 (2016).

11. J. Lian and M. Huang, "Evapotranspiration estimation for an oasis area in the Heihe River Basin using Landsat-8 images and the METRIC model," *Water Resour. Manag.* **29**(14), 5157–5170 (2015).

12. Z. Li et al., "A review of current methodologies for regional evapotranspiration estimation from remotely sensed data," *Sensors-Basel* **9**(5), 3801–3853 (2009).

13. K. Wang and E. Dickinson, "A review of global terrestrial evapotranspiration: observation, modeling, climatology, and climatic variability," *Rev. Geophys.* **50**(2), RG2005 (2012).

14. W. P. Kustas, "Estimates of evapotranspiration with a one-and two-layer model of heat transfer over partial canopy cover," *J. Appl. Remote Sens.* **29**(8), 704–715 (2010).

15. J. Yin and H. Wang, "Regional evapotranspiration estimation based on a two-layer remote-sensing scheme in Shahe River basin," *IOP Conf. Series Earth Environ. Sci.* **17**, 012141 (2014).

16. A. Were et al., "Aggregating spatial heterogeneity in a bush vegetation patch in semi-arid SE Spain: a multi-layer model versus a single-layer model," *J. Hydrol.* **349**(1–2), 156–167 (2008).

17. A. P. Schreinermcgraw et al., "Closing the water balance with cosmic-ray soil moisture measurements and assessing their relation to evapotranspiration in two semiarid water-sheds," *Hydrol. Earth Syst. Sci.* **20**(4), 80–86 (2016).

18. Y. Yang et al., "Comparison of three dual-source remote sensing evapotranspiration models during the MUSOEXE-12 campaign: revisit of model physics," *Water Resour. Res.* **51**(5), 3145–3165 (2015).

19. M. Norman et al., "Source approach for estimating soil and vegetation energy fluxes in observations of directional radiometric surface temperature," *Agr. Forest Meteorol.* **77**(3–4), 263–293 (1995).

20. J. Shuttleworth and S. Wallace, "Evaporation from sparse crops- an energy combination theory," *Q. J. R. Meteorolog. Soc.* **111**, 839–855 (1985).

21. W. Yao et al., "Estimating the regional evapotranspiration in Zhalong wetland with the two-source energy balance (TSEB) model and Landsat7/ETM+ images," *Ecol. Inform.* **5**(5), 348–358 (2010).

22. D. Kool et al., "A review of approaches for evapotranspiration partitioning," *Agr. Forest Meteorol.* **184**(1), 56–70 (2014).

23. A. Subedi and J. L. Chavez, "Crop evapotranspiration (ET) estimation models: a review and discussion of the applicability and limitations of ET methods," *J. Agr. Sci.* **7**(6), 50–68 (2015).

24. R. Tang et al., "An application of the Ts-VI triangle method with enhanced edges determination for evapotranspiration estimation from MODIS data in arid and semi-arid regions: implementation and validation," *Remote Sens. Environ.* **114**(3), 540–551 (2010).

25. Z. Sun et al., "Development of a simple remote sensing evapotranspiration model (Sim-ReSET): algorithm and model test," *J. Hydrol.* **376**(3-4), 476–485 (2009).

26. Z. Sun et al., "Further evaluation of the Sim-ReSET model for et estimation driven by only satellite inputs," *Hydrolog. Sci. J.* **58**(5), 994–1012 (2013).

27. R. Zhang et al., "An operational two-layer remote sensing model to estimate surface flux in regional scale: physical background," *Sci. China Ser. D* **48**(z1), 225–244 (2005).

28. R. Zhang et al., "Two improvements of an operation al two-layer model for terrestrial surface heat flux retrieval," *Sensors-Basel* **8**(10), 6165–6187 (2008).

29. J. Tian et al., "Application of an operational two-layer model for soil evaporation and vegetation transpiration retrievals in North China," *Geogr. Res.* **28**(5), 1297–1306 (2009).
30. Y. Liu et al., "Urban surface heat flux inversion based on infrared remote sensing and the relationship with land cover," *Acta Geogr. Sin.* **67**(1), 101–112 (2012).
31. M. Galleguillos et al., "Comparison of two temperature differencing methods to estimate daily evapotranspiration over a Mediterranean vineyard watershed from ASTER data," *Remote Sens. Environ.* **115**(6), 1326–1340 (2011).
32. D. Wu et al., "Evaluation of spatiotemporal variations of global fractional vegetation cover based on GIMMS NDVI data from 1982 to 2011," *Remote Sens.* **6**(5), 4217–4239 (2014).
33. S. Liang, "Narrow band to broadband conversions of land surface albedo, I: algorithms," *Remote Sens. Environ.* **76**(2), 213–238 (2000).
34. F. Wang et al., "An improved mono-window algorithm for land surface temperature retrieval from Landsat 8 thermal infrared sensor data," *Remote Sens.* **7**(4), 4268–4289 (2015).
35. "Thermal Infrared Sensor (TIRS) data," *USGS*, https://landsat.usgs.gov/landsat-8-l8-operational-land-imager-oli-and-thermal-infrared-sensor-tirs (29 January 2014).
36. M. Sugita and W. Brutsaert, "Comparison of land surface temperatures derived from satellite observations with ground truth during FIFE," *Int. J. Remote Sens.* **14**(9), 1659–1676 (1993).
37. M. S. Moran et al., "Estimating crop water deficit using the relation between surface-air temperature and spectral vegetation index," *Remote Sens. Environ.* **49**(3), 246–263 (1994).
38. W. P. Kustas et al., "Effects of remote sensing pixel resolution on modeled energy flux variability of croplands in Iowa," *Remote Sens. Environ.* **92**(4), 535–547 (2004).
39. C. Zhan et al., "Quantitative estimation of land surface evapotranspiration in Taiwan based on MODIS data," *Water Sci. Eng.* **4**(3), 237–245 (2011).
40. E. Hurtado and J. A. Sobrino, "Daily net radiation estimated from air temperature and NOAA-AVHRR data: a case study for the Iberian Peninsula," *Int. J. Remote Sens.* **22**(22), 1521–1533 (2001).
41. Y. Huang and K. Bi, "Methods for estimating surface total solar radiation based on Elman neural network," *J. Anhui Agric. Sci.* **39**(8), 4700–4702 (2011).
42. W. Kohsiek et al., "Saturation of the large aperture scintillometer," *Bound-Lay. Meteorol.* **121**(1), 111–126 (2006).
43. Z. Su, "The surface energy balance system (SEBS) for estimation of turbulent heat fluxes," *Hydrol. Earth Syst. Sci.* **6**(1), 85–100 (2002).
44. B. Wu et al., "Basin-wide evapotranspiration management: concept and practical application in Hai Basin, China," *Agric. Water Manage.* **145**, 145–153 (2014).
45. R. Allen et al., "Satellite-based energy balance for mapping evapotranspiration with internalized calibration (METRIC)—model," *J. Irrig. Drain. Eng.* **133**(4), 380–394 (2007)
46. W. Bastiaanssen et al., "A remote sensing surface energy balance algorithm for land (SEBAL). 1. Formulation," *J. Hydrol.* **212**–**213**(1–4), 198–212 (1998)
47. Z. Jia et al., "Validation of remotely sensed evapotranspiration over the Hai River Basin, China," *J. Geophys. Res.* **117**(D13), 13113 (2012).
48. B. Wu et al., "Validation of ET-Watch using field measurements at diverse landscapes: a case study in Hai Basin of China," *J. Hydrol.* **436**–**437**, 67–80 (2012).

Jian Yin is an associate professor at Northeast Agricultural University. He received his BS degree in geographical information science from Wuhan University in 2008, and his PhD degree in environmental science from Beijing Normal University in 2013. His current research interests include remote sensing, hydrology, and landscape science.

Biographies for the other authors are not available.

Queries

1. Please review the revised proof carefully to ensure your corrections have been inserted properly and to your satisfaction.

2. If any of your requested changes were not made on this revised proof, it's possible that they were in conflict with the journal's style. For example, author corrections to hyphenation, italics, and capitalization occasionally conflict with journal style. However, if you find that any corrections have been omitted that affect the technical content of your paper, please contact journals@spie.org and also include those corrections in your author response to the proofs.

3. Please check and confirm corresponding author affiliations.

4. Please check and confirm reference 35.